Journal of Materials Chemistry A

PAPER

View Article Online
View Journal | View Issue

Check for updates

Cite this: J. Mater. Chem. A, 2025, 13, 38290

Electrochemical production of H_2O_2 on palladium-based clusters driven by metal–support interaction

Prabhu Bharathan,[a] Can Li,[b] Bo Zhao,[c] Anna Dennett,[a] Lihua Zhang *[d] and Jiye Fang *[ab]

Utilizing palladium (Pd) clusters as active sites offers a promising route to minimize noble metal consumption in electrochemical hydrogen peroxide (H_2O_2) production. In this work, we present a synthesis approach for anchoring Pd-based clusters onto carbon-supported CeO_2 nanosubstrates to enable efficient H_2O_2 generation *via* the two-electron oxygen reduction reaction (ORR) pathway. By systematically adjusting Pd loading, we evaluated its impact on H_2O_2 yield and production rate. The catalyst with the lowest Pd content (0.027 wt%) exhibited outstanding performance, achieving 97% H_2O_2 selectivity, 94.2 faradaic efficiency at 0.7 V *vs.* RHE, and a peak production rate of 195.8 mol g_{Pd}^{-1} h^{-1}. A formulation containing 0.35 wt% Pd delivered a peak ORR mass activity nearly three times as high as that of commercial 10 wt% Pd/C, while retaining comparable electrochemical stability. These enhancements are attributed to synergistic effects among isolated PdO clusters, CeO_2 nanocrystals, and the conductive carbon support, which together facilitate oxygen adsorption and promote the two-electron ORR pathway. Analysis after accelerated durability testing further revealed a tendency toward cluster agglomeration and mass transfer from smaller to larger nanocrystals, indicative of a coarsening mechanism. Overall, this study underscores the promise of low-Pd PdO–CeO_2–carbon hybrid catalysts for scalable and efficient H_2O_2 electrosynthesis, while highlighting stability as a critical area for future improvement.

Received 17th July 2025
Accepted 8th October 2025

DOI: 10.1039/d5ta05763a

rsc.li/materials-a

Open Access Article. Published on 08 October 2025. Downloaded on 4/2/2026 11:09:37 PM.
This article is licensed under a Creative Commons Attribution-NonCommercial 3.0 Unported Licence.

Introduction

Hydrogen peroxide (H_2O_2), a valuable fuel and eco-friendly oxidant, plays a crucial role in a wide range of applications with minimal environmental impact. It is widely used across various fields, including the chemical industry, medicine, sterilization, wound healing, rocket propulsion, wastewater treatment, and other environmental processes.[1–3] While traditional preparation methods like the energy-intensive anthraquinone redox process[4] and direct synthesis from hydrogen (H_2) and oxygen (O_2), which can be hazardous,[5] are commonly employed, the electrochemical synthesis of H_2O_2 *via* two-electron oxygen reduction reaction (2e-ORR), as an environmentally friendly route, has gained significant attention as a safer and more energy-efficient alternative.[6–8]

Under alkaline conditions, O_2 can be electrochemically reduced either to hydroperoxide (HO_2^-) and hydroxide (OH^-) anion *via* a 2e-ORR pathway ($O_2 + H_2O + 2e^- \rightarrow HO_2^- + OH^-$), or directly to hydroxide ions through a four-electron ORR (4e-ORR) mechanism ($O_2 + 2H_2O + 4e^- \rightarrow 4OH^-$). A major challenge in H_2O_2 production *via* the 2e-ORR pathway is the competing 4e-ORR process, along with the possibly further cleavage of the O–O bond in the generated H_2O_2.[9] Pd-based electrocatalysts are widely used for efficient 2e-ORR synthesis of H_2O_2 due to their excellent selectivity and high catalytic activity, as well as their optimal HOO* binding energy and low overpotential compared to other catalysts.[7,10–12]

The primary advantage of using palladium (Pd) single atoms or small clusters over Pd nanoparticles (NPs) lies in the maximized utilization of catalytic atoms. In single-atom catalysts (SACs) or cluster catalysts, nearly every metal atom is exposed and available for catalytic activity, unlike in NPs, where a substantial fraction of atoms remain buried within the core and are thus catalytically inactive.[13] This leads to higher atomic efficiency and a reduced need for precious metals.[14,15] While SACs offer exceptional dispersion, they often suffer from structural instability, such as surface migration and aggregation, due to their high surface free energy.[16] In contrast, metal clusters, such as Pd clusters, represent a practical compromise, retaining high atom utilization while offering improved structural stability.[17] Moreover, as noted above, both Pd SACs and small clusters have been reported to favor the 2e-ORR

[a]Materials Science and Engineering Program, State University of New York at Binghamton, Binghamton, New York 13902, USA
[b]Department of Chemistry, State University of New York at Binghamton, Binghamton, New York 13902, USA. E-mail: jfang@binghamton.edu
[c]College of Arts & Sciences Microscopy, Texas Tech University, Lubbock, Texas 79409, USA
[d]Center for Functional Nanomaterials, Brookhaven National Laboratory, Upton, New York 11973, USA. E-mail: lhzhang@bnl.gov

This journal is © The Royal Society of Chemistry 2025

Open Access Article. Published on 08 October 2025. Downloaded on 4/2/2026 11:09:37 PM. This article is licensed under a Creative Commons Attribution-NonCommercial 3.0 Unported Licence.

pathway,[7,18,19] which preserves the O–O bond and enables high product selectivity. This level of selectivity is generally not achievable with larger NPs, which promote O–O bond cleavage *via* ensemble effects, thereby favoring the less selective 4e-ORR.[20]

To prevent the aggregation of Pd-based clusters, the use of a catalyst support is essential. Although a variety of supporting substrates are compatible with Pd nanostructures, we prefer to disperse Pd-based clusters on reducible supports, such as titania (TiO_2), vanadium pentoxide (V_2O_5), and ceria (CeO_2), rather than on non-reducible supports like silica (SiO_2) and magnesium oxide (MgO). This preference is due to the stronger metal–support interaction (MSI),[21] provided by reducible supports, which play a crucial role in the catalytic activity and product selectivity.[22] Previous studies have shown that the MSI between platinum (Pt) NPs and nanostructured CeO_2 can be significantly enhanced by two key factors: electron transfer from the Pt NPs to the support and oxygen transfer from nanostructured CeO_2 to the Pt surface *via* close interfacial contact.[23] These interactions help explain the observed improvements in catalytic performance. Additionally, CeO_2 nanocrystals (NCs) have been reported to function as a "nanoglue", effectively anchoring individual Pt atoms and thereby serving as an excellent substrate for SACs.[24,25] Moreover, cubic CeO_2 NCs have been shown to promote electrocatalytic activity toward the 2e-ORR pathway further.[26]

Based on these advantages, we systematically loaded content-dependent Pd clusters onto nanostructured CeO_2 substrates and investigated their performance in the electrochemical synthesis of H_2O_2, using carbon as the conducting additive. In practice, the assembly sequence of Pd, CeO_2, and activated carbon plays a crucial role in optimizing H_2O_2 production, as different loading sequences can lead to varying Pd loading fractions and spatial distributions across the components. Taking into consideration the MSI between Pd and CeO_2, the potential interaction between Pd and carbon, and insights from our preliminary evaluations, we developed a specific loading protocol for this study, as illustrated in Scheme 1.

Experimental section

Chemicals and materials

Sodium borohydride ($NaBH_4$, ≥98.0%), oleic acid (90%), toluene (99.8%), sodium hydroxide (NaOH, ≥95%), anhydrous isopropanol (99.5%), Nafion® 117 solution (5%), and Pd/C catalyst containing 10 wt% Pd (referred to as "Pd_{10}/C") were purchased from Millipore Sigma. Cerium(III) nitrate hexahydrate ($Ce(NO_3)_3 \cdot 6H_2O$, 99.5%), palladium(II) chloride ($PdCl_2$, 99%), *tert*-butylamine (>98%), hexane (≥98.5%), anhydrous potassium hydroxide (KOH, ≥99.95%), and anhydrous ethanol (Koptec, 200 proof) were sourced from Alfa Aesar, Acros, TCI, BDH, Fischer, and Decon Labs, Inc., respectively. Ketjen Black EC-600JD was provided by Lion Specialty Chemicals Co., Ltd (JP). Ultrapure water with a resistivity of 18.2 MΩ cm was obtained from a Purelab Flex3 water purification system (ELGA, UK).

Synthesis of CeO_2 nanocrystals

CeO_2 NCs were synthesized using a previously reported procedure for nanocube formation.[27,28] Briefly, 7.5 mL of cerium nitrate solution (16.7 mM), 7.5 mL of toluene, 0.75 mL of oleic acid, and 75 μL of *tert*-butylamine were combined and transferred into a 15 mL Teflon-lined stainless steel autoclave. The autoclave was then placed in a pre-heated oven at 180 °C and maintained at this temperature for 24 hours. After the reaction, the autoclave was removed from the oven and allowed to cool to room temperature. The turbid upper layer of the resulting mixture was isolated using a separatory funnel, washed with a 1 : 2 (v/v) mixture of hexane and ethanol, and collected by centrifugation at 9000 rpm. The resulting precipitate was redispersed in hexane and re-cleaned for two more similar cycles. CeO_2 NCs were stored in hexane dispersions, and the formation yield was calculated based on the CeO_2 mass obtained after drying the suspension.

Synthesis of $Pd_{cluster}$–CeO_2/C catalysts

An appropriate amount of Ketjen-black carbon was dispersed in ethanol under sonication for at least 30 minutes. This dispersion was then combined with a hexane suspension of CeO_2 NCs and further sonicated for an additional 2 hours. The resulting mixture was left undisturbed for 12 hours to allow diffusion and adsorption of the CeO_2 NCs onto the carbon surface. The composite was subsequently collected by centrifugation and dried overnight in a vacuum oven. The carbon-supported CeO_2 NCs (designated as CeO_2/C) were then washed multiple times with an ethanol solution containing 0.1 M NaOH to remove residual oleic acid. After washing, the solid composite was collected by centrifugation and finally dried in a vacuum oven. The dried CeO_2/C support was annealed in air at 300 °C for 12 hours in a tube furnace to ensure complete removal of any

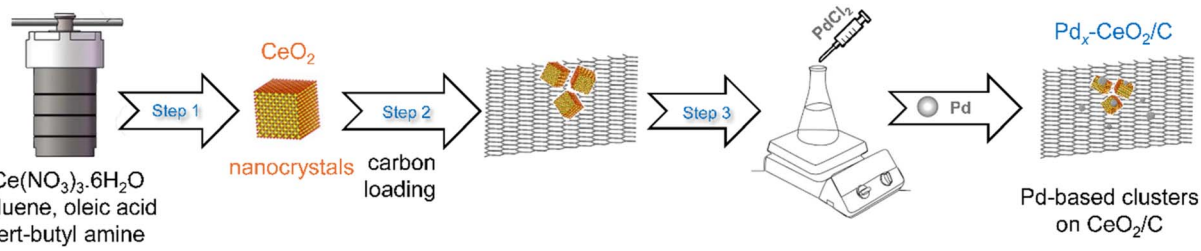

Scheme 1 Schematic illustration of the synthetic steps in the preparation of nanoclustered Pd_x–CeO_2/C.

Open Access Article. Published on 08 October 2025. Downloaded on 4/2/2026 11:09:37 PM. This article is licensed under a Creative Commons Attribution-NonCommercial 3.0 Unported Licence.

remaining organics. The final CeO_2 loading on CeO_2/C was adjusted to approximately 60 wt%.

Next, a pre-determined amount of the heated CeO_2/C was dispersed in 10 mL of ultrapure water under sonication to form a uniform suspension. A specified volume of $PdCl_2$ aqueous suspension was then introduced to the system under magnetic stirring. Subsequently, an appropriate amount of $NaBH_4$ aqueous solution (0.01 M) was added dropwise under vigorous stirring to reduce Pd ions discretely. The exact volume of $PdCl_2$ solution depended on the target Pd loading in the final Pd–CeO_2/C catalysts, with adjustments made based on Pd content remaining in the supernatant, as determined by inductively coupled plasma-optical emission spectrometry (ICP-OES, *vide infra*). However, the molar ratio of added $PdCl_2$ to $NaBH_4$ was consistently maintained at 1 : 1.5 to maximize Pd ion reduction. The reaction mixture was separated by centrifugation at 9000 rpm. The supernatant was retained for ICP-OES analysis to determine Pd loss during processing, while the resulting catalysts, designated as $Pd_{cluster}$–CeO_2/C, were dried in a vacuum oven and then annealed in air at 300 °C for 30 minutes in a tube furnace. Hereafter, the $Pd_{cluster}$–CeO_2/C is denoted as Pd_x–CeO_2/C, where x represents the actual Pd content (wt%) relative to the total mass of the catalyst, calculated from the difference between the input Pd amount and the residual Pd in the supernatant as measured by ICP-OES. Compared to an alternative Pd-loading sequence presented in the "Results and discussion" section, this preparation method is referred to as "post-loading".

Working electrode preparation

To prepare the catalyst ink, 5.0 mg of Pd_x–CeO_2/C was dispersed in a mixture of ultrapure water (0.6 mL), isopropanol (0.4 mL), and 5% Nafion® solution (10.0 μL), followed by ultrasonication for 1 hour. Then, 30.0 μL of the resulting ink was drop-cast onto a pre-cleaned glassy carbon (GC) rotating disk electrode (RDE, 5 mm diameter; Pine Research Instrumentation) and dried at room temperature under ambient pressure.

To prepare the ink of the Pd/C standard catalyst, 1.5 mg of benchmark Pd_{10}/C (10 wt% Pd on activated carbon) was dispersed in a mixture of ultrapure water (0.6 mL), isopropanol (0.4 mL), and 5% Nafion® solution (10.0 μL), followed by ultrasonication for 1 hour. Then, 26.4 μL of the resulting ink was drop-cast onto the same GC electrode, resulting in a Pd loading of 20.0 μg cm^{-2} on the RDE.

The H_2O_2 selectivity during the ORR was evaluated using a rotating ring-disk electrode (RRDE; Pine Research Instrumentation) with a GC geometric surface area of 0.196 cm^2. For these measurements, 30.0 μL of catalyst ink containing Pd_x–CeO_2/C (x = 0.027, 0.25, 0.35, 0.76, and 1.53) or 26.4 μL of ink containing the benchmark Pd_{10}/C was drop-cast onto the RRDE and dried at room temperature under atmospheric pressure prior to electrochemical characterizations.

Electrochemical measurements

RDE-based electrochemical measurements were conducted at ambient conditions using a Gamry 1000E electrochemical workstation equipped with a standard three-electrode system. The working electrode (GC RDE) was coated with the drop-cast catalyst as mentioned above. A Ag/AgCl wire electrode immersed in saturated 4 M KCl served as the reference electrode, and a graphite rod was used as the counter electrode. All measured potentials ($E_{Ag/AgCl}$) were converted to the reversible hydrogen electrode (RHE) scale using the following equation:

$$E_{RHE} = E_{Ag/AgCl} + 1.0258\ (V)$$

A custom-made polycarbonate electrochemical cell was used to house the electrodes and electrolyte for ORR, accelerated durability tests (ADTs), and RRDE measurements. Initially, the RDE was cycled for ~50 potential sweeps between −0.9 V and 0.2 V *vs.* Ag/AgCl at a scan rate of 50 mV s^{-1} and a step size of 10 mV in N_2-saturated 1 M KOH solution. This step was performed to activate the catalyst by removing residual surface ligands and stabilizing the cyclic voltammetry (CV) profiles.

Following activation, ORR measurements were carried out in fresh O_2-saturated 1 M KOH *via* cathodic scanning over the same potential window at the same scan rate and step size, and rotation speeds of 400, 625, 900, 1225, 1600, and 2025 rpm, respectively.

ADTs were performed by cycling the potential between −0.4258 V and −0.0258 V *vs.* Ag/AgCl at a scan rate of 100 mV s^{-1} and step size of 20 mV in O_2-saturated 1 M KOH. The cycling was repeated in 5000-cycle increments until the current at the half-wave potential ($E_{1/2}$) dropped to 60% of its initial value. To minimize contamination, a fresh O_2-saturated electrolyte was used after every 5000 cycles.

The number of electrons transferred in the ORR reaction was calculated using the Koutecký–Levich plots (J^{-1} *vs.* $\omega^{-1/2}$, J is the measured current density and ω is the rotation speed of RDE) using the data acquired at various electrode potentials (*i.e.*, 0.60, 0.70, 0.80, and 0.85 V). A linear fit of the Koutecký–Levich plot gave the slope, related to the Levich constant, as:

$$\frac{1}{k_{slope}} = B = 0.62nFC_0(D_0)^{\frac{2}{3}}\nu^{\frac{-1}{6}}$$

where k_{slope} is the electron-transfer rate constant, B is the Levich constant, n is the transferred electron number, F is the Faraday constant, C_0 is the bulk concentration of oxygen (1.22×10^{-6} mol cm^{-3}), D_0 is the diffusion coefficient of oxygen in 1 M KOH (1.95×10^{-5} cm^2 s^{-1}), ν is the kinematic viscosity of 1 M KOH solution (9.97×10^{-3} cm^2 s^{-1}).

The kinetic current (j_k)at 0.85 V *vs.* RHE was calculated using the diffusion limiting current density (j_L) and the total current (j) through the equation.

$$j_k = \frac{j_L \times j}{j_L - j}$$

The ORR mass activity of a catalyst at 0.85 V *vs.* RHE was calculated by normalizing the kinetic current (derived from the Koutecký–Levich equation) at 0.85 V *vs.* RHE to the mass of Pd element deposited on the GC electrode.[29,30] The ORR catalytic yield toward H_2O_2 was evaluated using Gamry 1000E and 1010E

 This journal is © The Royal Society of Chemistry 2025

Open Access Article. Published on 08 October 2025. Downloaded on 4/2/2026 11:09:37 PM. This article is licensed under a Creative Commons Attribution-NonCommercial 3.0 Unported Licence.

potentiostats with an RRDE in O_2-saturated 1 M KOH solution, at a scan rate of 5 mV s^{-1} and a rotation speed of 1600 rpm. A potential of 1.4 V (*vs.* RHE) was applied to the Pt ring electrode to oxidize the H_2O_2 produced at the catalyst-coated disk. The duration of measurements of both the ring and risk electrodes was kept identical. The collection efficiency (N) of the Pt-ring electrode was experimentally calibrated to be 0.37. The number of electrons transferred (n) and the yield toward H_2O_2 were calculated using the following equations:[9,31,32]

$$n = \frac{4i_d}{i_d + \frac{i_r}{N}}$$

$$H_2O_2\ \text{selectivity}(\%) = \frac{\frac{i_r}{N}}{\left(|i_d| + \frac{i_r}{N}\right)} \times 200$$

$$\text{Faradaic efficiency}(FE)\text{of } H_2O_2(\%) = \frac{\frac{i_r}{N}}{|i_d|} \times 100$$

where i_d is the disc current, and i_r is the ring current.

Other characterizations

X-ray diffraction (XRD) patterns were collected using a PANalytical X'Pert Pro diffractometer with a scan rate of 0.96° min^{-1} and a step size of 0.016° over the 2θ range of 25° to 60° or 70°. X-ray photoelectron spectroscopy (XPS) was performed on a PHI 5000 VersaProbe system (Physical Electronics Inc.). Transmission electron microscopy (TEM) images were acquired with a JEOL JEM-2100F field-emission microscope operating at 200 kV. High-angle annular dark-field scanning transmission electron microscopy (HAADF-STEM) images, high-resolution TEM (HRTEM) images, and energy-dispersive X-ray spectroscopy (EDX) maps were obtained using a Thermo Fisher Talos 200X. For STEM and EDX analyses, hexane suspensions of the samples were drop-cast onto amorphous carbon-coated copper (Cu) grids and dried under ambient conditions. Pd compositions were determined by ICP-OES (PerkinElmer Optima 7000 DV).

Results and discussion

Composition, crystallinity, and valence state investigation

The Pd-component distribution in the as-synthesized Pd_x–CeO_2/C samples was investigated using HAADF-STEM imaging combined with EDX elemental mapping. Fig. 1 presents data for a representative sample with an actual Pd loading of 1.53 wt% relative to the total sample mass ($Pd_{1.53}$–CeO_2/C). A low-magnification HAADF-STEM image is shown in Fig. 1a (see also Fig. S1a), with the red-highlighted region enlarged in Fig. 1b. Elemental maps for C, Ce, O, and Pd corresponding to this region are shown in Fig. 1c–f, respectively, confirming a highly homogeneous distribution of each element. In

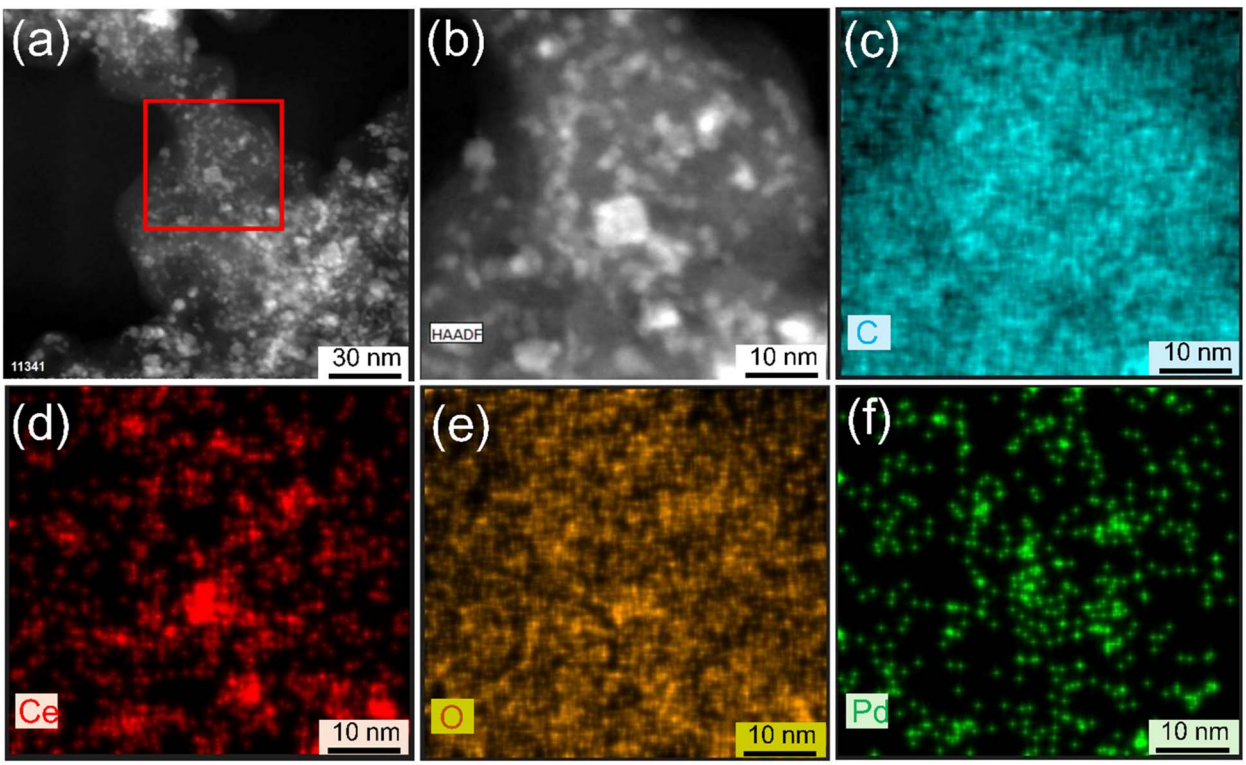

Fig. 1 HAADF-STEM images and EDX maps of catalyst $Pd_{1.53}$–CeO_2/C. (a) and (b), HAADF-STEM images with different magnifications; (c)–(f), EDX maps on the area shown in (b) for elements C, Ce, O, and Pd, respectively.

Open Access Article. Published on 08 October 2025. Downloaded on 4/2/2026 11:09:37 PM.
This article is licensed under a Creative Commons Attribution-NonCommercial 3.0 Unported Licence.

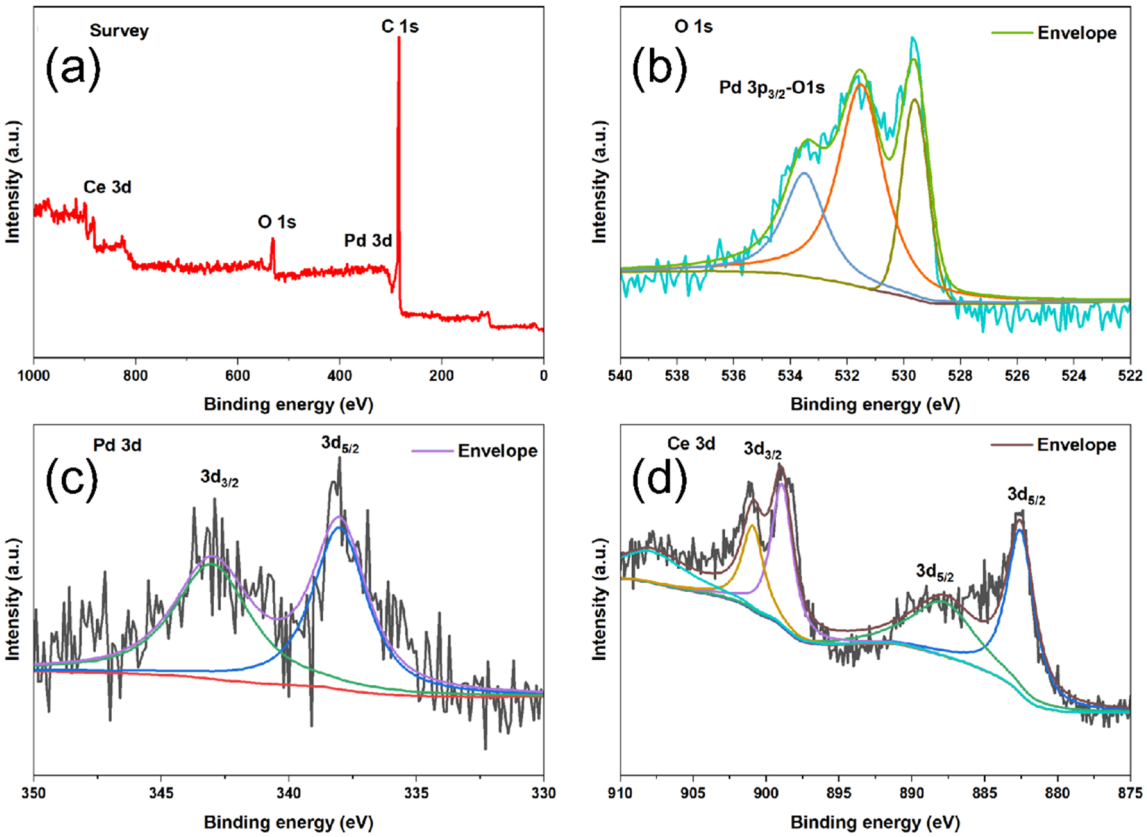

Fig. 2 XPS spectra of $Pd_{1.53}$–CeO_2/C. (a) Survey spectrum of $Pd_{1.53}$–CeO_2/C; (b)–(d) XPS spectra of Pd $3p_{3/2}$–O 1s (b), Pd 3d (c), and Ce 3d (d) from sample $Pd_{1.53}$–CeO_2/C.

particular, the Pd signal appears sparsely dispersed across both the CeO_2 and carbon supports. An HRTEM image of the same sample (Fig. S1b) reveals Pd-based crystalline clusters or NCs on CeO_2. Lattice fringe analysis of selected NCs yields an average spacing of 3.26 Å, closely matching the (111) plane of cubic PdO (3.26 Å, ICDD PDF card 46-1211). In contrast, the maximum lattice spacing for metallic Pd is only 2.246 Å for the (111) plane (ICDD PDF card 46-1043). This strongly indicates that the Pd species present on the CeO_2 NCs are predominantly in the oxidized PdO form rather than metallic Pd. For comparison, the TEM images of individual CeO_2 substrates that were synthesized using the same recipe are shown in Fig. S2.

All prepared samples ($x = 0.027$, 0.25, 0.35, 0.76, 1.53) were examined by XRD, which revealed no detectable metallic Pd or palladium oxide phases, as shown in Fig. S3. This suggests that no dominant Pd-based NCs are present on the CeO_2/C substrates, and the Pd element detected by EDX is most likely distributed as small clusters or individual atoms. To quantify the actual Pd loading in each sample, ICP-OES was used, and the results are summarized in Table S1.

To further examine the valence states of the elements on the sample surfaces, XPS analyses were performed. Fig. 2 shows the XPS spectra of $Pd_{1.53}$–CeO_2/C. The survey spectrum (Fig. 2a) confirms the presence of Pd, O, and Ce in the sample. The deconvoluted O 1s spectrum (Fig. 2b) reveals three distinct peaks at 529.4, 531.3, and 533.5 eV. The peaks at 529.4 and 531.3 eV correspond to lattice oxygen and surface oxygen,[33] respectively, while the peak at 533.5 eV is attributed to the Pd $3p_{3/2}$–O 1s doublet,[34] suggesting the formation of Pd–O bonds, likely in the form of Pd–O–Ce bridge on the CeO_2 substrate.[18] The Pd 3d spectrum (Fig. 2c) displays characteristic spin–orbit doublet coupling at 338.1 and 343.2 eV with a splitting of 5.1 eV, consistent with standard Pd^{2+} 3d binding energies. The absence of peaks near ~335.9 and ~340.9 eV suggests that Pd is likely not present in its metallic form on the surface of this sample, and presumably not on those samples containing smaller clusters, either. This conclusion is further supported by lattice fringe analysis from the HRTEM observations. Additionally, the Ce $3d_{5/2}$ and Ce $3d_{3/2}$ peaks (Fig. 2d) are deconvoluted into five peaks located at 882.5, 889.1, 898.8, 901.0, and 907.5 eV, exhibiting a spin–orbit splitting with a binding energy range of 25 eV, which is consistent with the CeO_2 phase.[33,35] These XPS results indicate that the $Pd_{1.53}$–CeO_2/C sample contains phase-pure CeO_2, along with surface Pd–O species, although no PdO crystallite signal was detected by XRD. In combination with the HRTEM observation discussed above, it can be inferred that Pd-based clusters are anchored on the surface of CeO_2 NCs through chemical bonding, potentially also interacting with carbon, and that PdO is present on the surface.

General electrocatalytic performance

To investigate the electrocatalytic performance of the Pd-based catalysts, the samples were first loaded onto the GC-RDE and

 This journal is © The Royal Society of Chemistry 2025

Open Access Article. Published on 08 October 2025. Downloaded on 4/2/2026 11:09:37 PM.
This article is licensed under a Creative Commons Attribution-NonCommercial 3.0 Unported Licence.

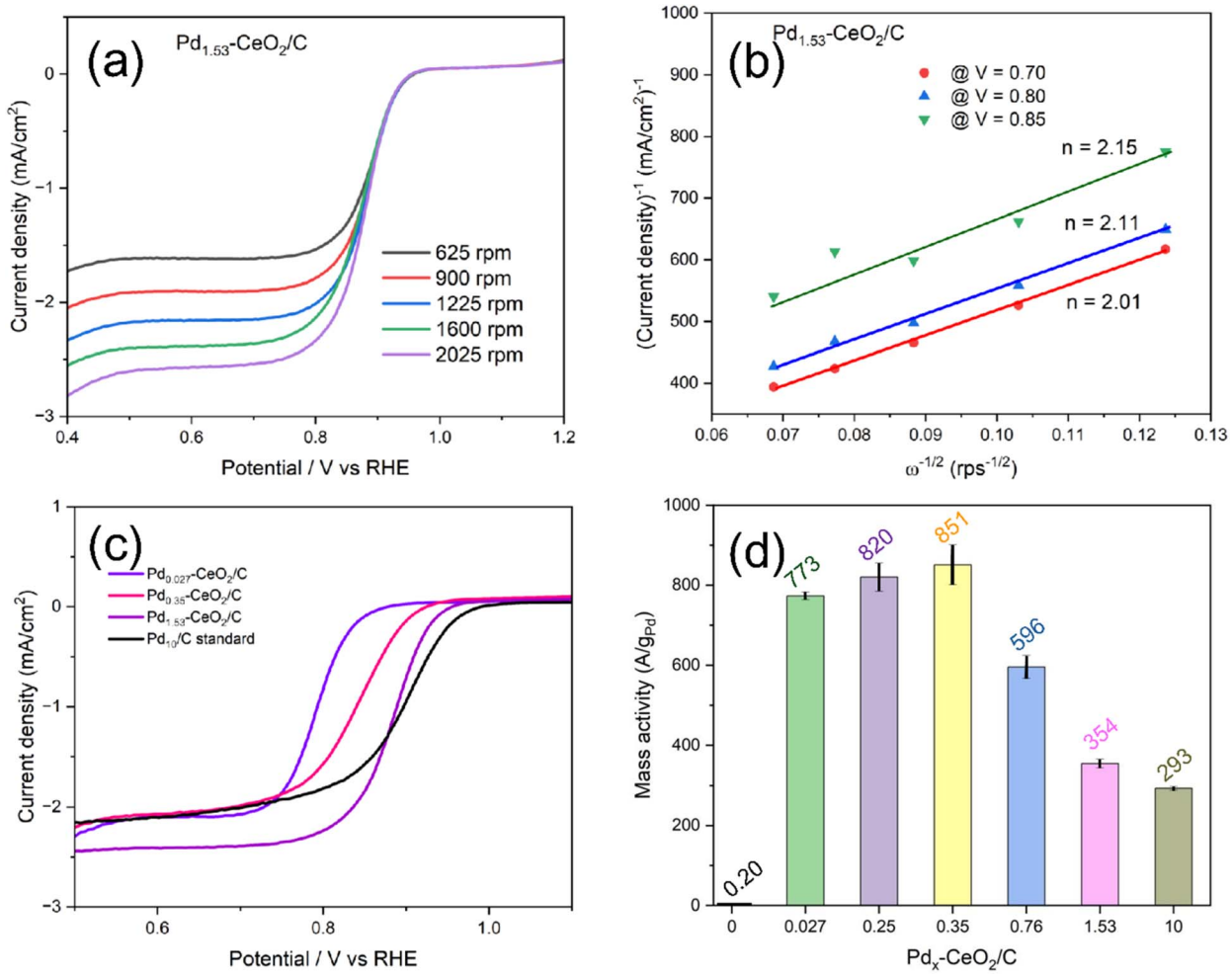

Fig. 3 Electrocatalytic performance of Pd_x–CeO_2/C toward H_2O_2 production. (a) ORR polarization curves of $Pd_{1.53}$–CeO_2/C at various rotation speeds; (b) Koutecký–Levich plots (j^{-1} *vs.* $\omega^{-1/2}$) using ORR polarization data $Pd_{1.53}$–CeO_2/C; (c) ORR polarization curves of other Pd_x–CeO_2/C and benchmark Pd_{10}/C at a rotation speed of 1600 rpm in 1 M KOH solution; (d) calculated mass activity (at 0.85 V *vs.* RHE) toward ORR of Pd_x–CeO_2/C and Pd_{10}/C.

electrochemically activated by potential cycling. The cycling was conducted in N_2-saturated 1 M KOH solution, scanning from 0.15 to 1.2 V *vs.* RHE at a rate of 50 mV s^{-1} with a step size of 10 mV, until the CV profiles stabilized. Fig. S4a shows representative stabilized CV profiles of $Pd_{1.53}$–CeO_2/C and $Pd_{1.84}$/C (*vide infra*) after 50 potential cycles. Once stable CVs were achieved, the ORR characteristics of the samples were assessed in O_2-saturated 1 M KOH solution. As an example, Fig. 3a presents the ORR polarization curves of $Pd_{1.53}$–CeO_2/C recorded at various RDE rotation speeds ranging from 625 to 2025 rpm. The corresponding Koutecký–Levich plots, based on current densities at 0.70, 0.80, and 0.85 V, are shown in Fig. 3b. The slopes of the linear fits were used to calculate the electron transfer number (n), which was found to be close to 2. This indicates that the ORR follows a 2e-ORR pathway, resulting in the production of H_2O_2. This behavior was consistently observed across various Pd-loading Pd_x–CeO_2/C, confirming that the n remains close to 2 regardless of Pd content within the explored range. These results align with prior reports on Pd-based catalysts that lack extended bulk or ensemble sites.[15] The mechanism of H_2O_2 generation on Pd clusters has also been previously discussed.[36] Further exploration was carried out using a series of Pd-loading variants of CeO_2/C, specifically, Pd_x–CeO_2/C with x = 0.027, 0.35, and 1.53 wt%. Their ORR polarization curves were compared with that of a benchmark Pd_{10}/C catalyst, as shown in Fig. 3c. The $E_{1/2}$ of the benchmark Pd_{10}/C was measured as 0.8925 V *vs.* RHE. In comparison, the Pd_x–CeO_2/C samples exhibited $E_{1/2}$ values of 0.790, 0.840, and 0.875 V *vs.* RHE, respectively, with $Pd_{1.53}$–CeO_2/C showing the highest $E_{1/2}$ among the three, approaching that of Pd_{10}/C. Based on the actual Pd loading in each sample, the ORR mass activity at 0.85 V *vs.* RHE was calculated, as illustrated in Fig. 3d. Notably, $Pd_{0.35}$–CeO_2/C exhibited the highest mass activity, approximately three times as high as that of Pd_{10}/C. This enhanced performance may be attributed to the optimized distribution of Pd-containing species at the cluster level in $Pd_{0.35}$–CeO_2/C, compared to the nanocrystalline Pd domains in Pd_{10}/C. Additionally, the strong MSI in $Pd_{0.35}$–CeO_2/C may induce a downward shift in the Pd d-band center, thereby optimizing OH^--desorption energy from the catalyst surface sites.[37]

Open Access Article. Published on 08 October 2025. Downloaded on 4/2/2026 11:09:37 PM. This article is licensed under a Creative Commons Attribution-NonCommercial 3.0 Unported Licence.

H_2O_2 production study

To directly evaluate the selectivity of H_2O_2 production *via* the 2e-ORR pathway, RRDE measurements were conducted on the Pd_x–CeO_2/C catalysts. Unlike conventional RDE, RRDE employs a Pt-ring electrode in addition to the GC disk, enabling real-time detection and quantification of H_2O_2 generated during ORR on the disk. This setup provides critical insights into the reaction pathway, reaction kinetics, and H_2O_2 selectivity. The RRDE experiment involves the independent control of two potentiostat channels, one for the disk and one for the ring, both sharing the same reference and counter electrodes. During testing, both disk and ring currents were simultaneously recorded for each sample. Among the tested catalysts, $Pd_{0.027}$–CeO_2/C exhibited the highest ring current, ~0.10 mA greater than that of the benchmark Pd_{10}/C, and ~0.07 mA higher than those of the other Pd_x–CeO_2/C catalysts across the tested potential range, as shown in Fig. S5. This indicates a higher peroxide oxidation current and, consequently, a greater H_2O_2 generation capacity for $Pd_{0.027}$–CeO_2/C. The ring currents of the other catalysts fell between these values. Based on the disk and ring currents, the *n* for $Pd_{0.027}$–CeO_2/C was calculated to be ~2 at potentials below 0.7 V *vs.* RHE, while the *n* values for the other Pd_x–CeO_2/C catalysts ranged between 2 and 3, as illustrated in Fig. 4a. This result indicates that *n* is closely correlated with Pd loading, and more specifically, with the fraction of Pd-containing species present as clusters. These findings are consistent with the RDE-derived results in Fig. 3b, reinforcing that the 2e-ORR pathway is predominant in these systems. Note that the slight discrepancy in *n* values between Fig. 3b and 4a arises from the use of different measurement methods (*e.g.*, RDE *vs.* RRDE for $Pd_{1.53}$–CeO_2/C). Correspondingly, Fig. 4b shows that the H_2O_2 selectivity increases as Pd loading decreases, likely due to a higher fraction of isolated Pd-based clusters, following a trend similar to that reported for ultra-low-Pd-loading SACs.[15] Notably, $Pd_{0.027}$–CeO_2/C exhibits the highest H_2O_2 selectivity among all tested samples, achieving 93.2% and 97.0% at 0.6 and 0.7 V *vs.* RHE, respectively, with corresponding *FE* of 87.3% and 94.2%. A similarly enhanced H_2O_2 selectivity of single-atom Pd of rod-like CeO_2, compared to Pt NPs on the same support, has also been reported recently.[38] Theoretically, it has been predicted that the oxidation state of a Pd atom isolated on an oxide surface, such as γ-Al_2O_3 (100), can promote the electrochemical synthesis of H_2O_2.[39] The exceptional performance of $Pd_{0.027}$–CeO_2/C is attributed to its dominant 2e-ORR pathway, along with the synergistic MSI among Pd-based clusters, CeO_2, and the carbon support (*vide infra*), facilitated through oxygen bonding. These values substantially exceed those reported for Pd SAC on carbon nanotube (Pd-CNT), which delivered ~88.0% and 89.5% selectivity at 0.6 and 0.7 V *vs.* RHE in 0.1 M KOH, respectively,[40] and for Co SAC on graphene oxide (Co_1@GO), which exhibited 81.4% selectivity at 0.6 V *vs.* RHE in the same electrolyte.[41] Recent computational results also indicate that the Pd–O intermediate, stabilized by Cu, can enhance 2e-ORR activity at the Pd site.[42] Table S2 summarizes the estimated molar production rates of H_2O_2 for the Pd_x–CeO_2/C catalysts, assuming a two-electron transfer mechanism at the disk.

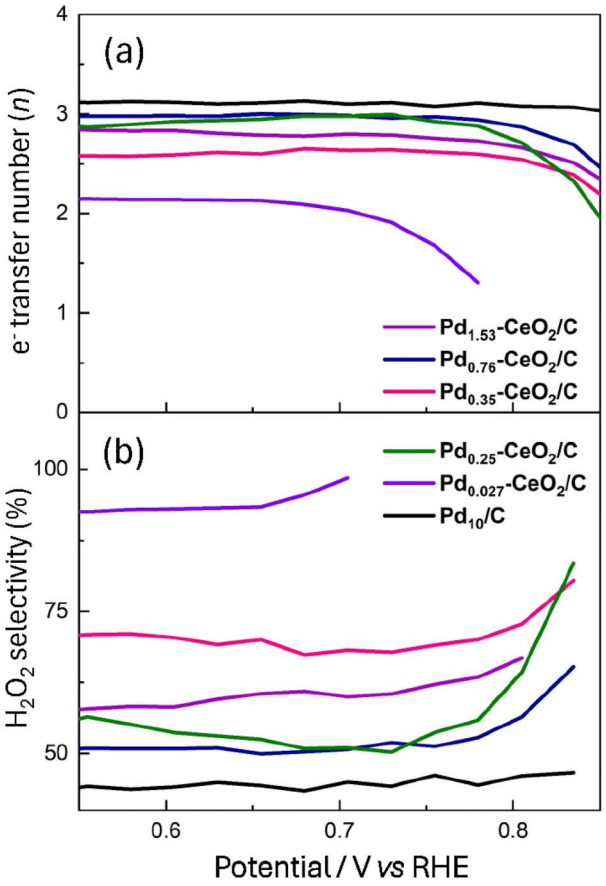

Fig. 4 ORR electron transfer numbers and H_2O_2 selectivity of Pd_x–CeO_2/C and Pd_{10}/C determined in 1 M KOH at a rotation speed of 1600 rpm using an RRDE system. (a) Determined electron transfer numbers; (b) H_2O_2 production selectivity.

It is noteworthy that while the highest H_2O_2 mass activity (851 A g^{-1}) was achieved with the $Pd_{0.35}$–CeO_2/C sample (Fig. 3d), the highest H_2O_2 selectivity (~97.0% at 0.7 V *vs.* RHE) was observed for $Pd_{0.027}$–CeO_2/C (Fig. 4b). The higher kinetic current of $Pd_{0.35}$–CeO_2/C (−0.83 mA cm^{-2} at 0.85 V *vs.* RHE), compared to that of $Pd_{0.027}$–CeO_2/C (−0.095 mA cm^{-2} at 0.85 V *vs.* RHE), accounts for its superior mass activity. In contrast, the enhanced H_2O_2 selectivity of $Pd_{0.027}$–CeO_2/C is attributed to its preference for the 2e-ORR pathway. As shown in Fig. 4a, $Pd_{0.027}$–CeO_2/C, which contains an extremely low Pd loading and thus lacks Pd ensemble sites, exhibits an *n* close to 2 – ideal for selective H_2O_2 production. Conversely, $Pd_{0.35}$–CeO_2/C, with higher Pd loading and a greater propensity for ensemble site formation, displays an *n* of ~2.5, indicative of a mixed 2e/4e-ORR pathway and resulting in reduced H_2O_2 selectivity. At a disc potential of 0.7 V *vs.* RHE, all Pd_x–CeO_2/C catalysts exhibit higher H_2O_2 production rates per gram of Pd than the benchmark Pd_{10}/C. Notably, $Pd_{0.027}$–CeO_2/C achieved H_2O_2 molar production rates of 205.6 and 195.8 mol g_{Pd}^{-1} h^{-1} at 0.6 and 0.7 V *vs.* RHE, respectively, significantly exceeding those of the other Pd_x–CeO_2/C catalysts with higher Pd fractions as well as recently reported PdCu nanocatalysts[42] and other transition metal SACs.[40,41,43,44] These values reflect the strong potential of

 This journal is © The Royal Society of Chemistry 2025

Open Access Article. Published on 08 October 2025. Downloaded on 4/2/2026 11:09:37 PM. This article is licensed under a Creative Commons Attribution-NonCommercial 3.0 Unported Licence.

these catalysts for practical H_2O_2 electrosynthesis.[9] For comparison, Table S3 presents the performance metrics of several recently reported state-of-the-art electrocatalysts for H_2O_2 production in alkaline media.

In addition to the remarkable enhancement in mass activity and H_2O_2 production performance, the Pd_x–CeO_2/C catalysts also demonstrated varying degrees of durability. To further assess their stability, ADTs were performed on all selected samples. The ADTs involved potential cycling between 0.6 and 1.0 V *vs.* RHE at a scan rate of 100 mV s^{-1} in 1 M KOH solution. For each sample, CV profiles and ORR polarization curves were recorded at a rotation speed of 1600 rpm both at the beginning and after 5000 cycles, using a freshly prepared O_2-saturated 1 M KOH solution. As an example, Fig. S4a and b show the CV and ORR polarization curves of $Pd_{1.53}$–CeO_2/C, respectively, revealing a noticeable decline in activity with a half-wave potential shift ($\Delta E_{1/2}$) of 110 mV after 5000 cycles. Fig. S4c includes the ORR polarization curves for all Pd_x–CeO_2/C samples, along with the benchmark Pd_{10}/C and pure CeO_2/C (*vide infra*). $Pd_{0.25}$–CeO_2/C and $Pd_{0.35}$–CeO_2/C exhibited relatively higher mass activity. However, their durability remains limited compared to that of the nanocrystalline benchmark catalyst, Pd_{10}/C. Fig. S4d illustrates the mass activity of all tested catalysts before and after ADTs, with the corresponding numerical data provided in Table S4. The observed decreases in mass activity after 5000 cycles are likely due to the aggregation of Pd-based clusters, which reduces the electrochemically active surface area. In addition, the potential dissolution of Pd-based clusters into the electrolyte may also contribute to the decline in activity.

To further verify this interpretation, we re-examined the catalyst samples after 5000 cycles of ADT. Low-magnification HAADF-STEM images of $Pd_{0.76}$–CeO_2/C and $Pd_{1.53}$–CeO_2/C (Fig. S6a and b) illustrate the distribution of NCs across relatively large areas. Elemental mapping revealed the presence of PdO NCs in the $Pd_{1.53}$–CeO_2/C sample (Fig. S6c–f), whereas such nanostructures were not observed in $Pd_{0.76}$–CeO_2/C (Fig. S6g–j). Notably, the size of PdO NCs in $Pd_{1.53}$–CeO_2/C prior to ADT (less than ~2 nm, Fig. 1f) was significantly smaller compared to those identified in the mapping images after ADT (Fig. S6c). This clearly indicates that ADT promotes the aggregation of PdO clusters in the higher-loading catalyst. Given that HRTEM enables detailed analysis of NCs, we examined the size and distribution of PdO NCs in the $Pd_{1.53}$–CeO_2/C catalyst, as shown in Fig. S7a and b. Analysis of the nearest-neighbor distances between PdO NCs suggests a tendency toward agglomeration and aggregation induced by ADT. Prior to cycling, the average interparticle distance was ~10 nm, which decreased to ~7 nm after 5000 cycles (Fig. S7c and d). In addition, the average size of the PdO NCs increased from ~4 to ~5 nm within the observed area (Fig. S7e and f), further indicating a possible onset of cluster coalescence. In other observed regions where agglomeration had already taken place, we found that the sizes of individual PdO NCs surrounding agglomerated groups (blue circles) were actually reduced (Fig. S8a). A comparison between Fig. S8a and b reveals that the more severe the agglomeration, the smaller the surrounding satellite NCs appear to be. This observation indicates a mass transfer process among NCs during ADT, analogous to the coarsening behavior commonly observed during thermal treatments[45] – specifically, the growth and aggregation of larger NCs at the expense of smaller ones. This behavior is characteristic of Ostwald ripening, driven by the higher surface energy and solubility of smaller NCs, along with the dynamic coexistence of clusters in close proximity. As a result, smaller NCs and clusters gradually dissolve, and their mass is redeposited onto larger NCs within the agglomerates. We further examined the lattice fringe of selected individual NCs, and found that the measured spacings were ~3.22 Å and ~2.80 Å (Fig. S8c and d), corresponding to the (111) and (200) planes of cubic PdO, respectively. These values are consistent with those observed prior to ADT (Fig. S1b), confirming that the PbO phase remains unchanged after cycling. No lattice fringes corresponding to metallic Pd were detected from these NCs.

To evaluate the H_2O_2 production yield degradation of $Pd_{0.027}$–CeO_2/C, the most promising catalyst, RRDE measurements were repeated after the catalyst underwent 5000 potential cycles under identical conditions. Fig. S9 presents the ORR polarization disc current (i_d), ring current (i_r), electron transfer number (n), and

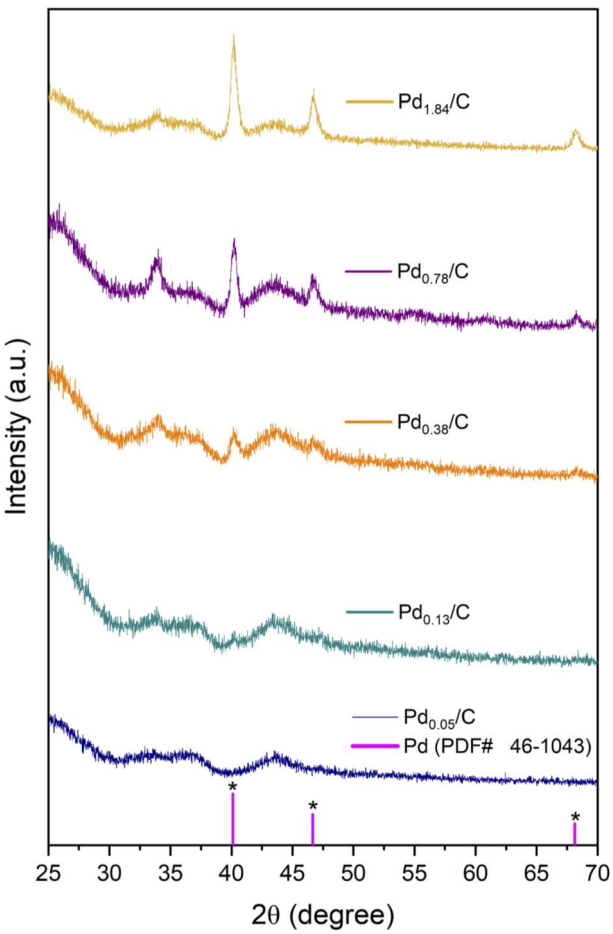

Fig. 5 XRD patterns of Pd_x/C (x = 0.05, 0.13, 0.38, 0.78, 1.84). The vertical lines, at 2θ = 40.119°, 46.659°, 68.121°, indicate the standard diffraction pattern of Pd (ICDD PDF card 46-1043). An apparent crystalline phase of Pd can be determined from $Pd_{1.84}$/C, $Pd_{0.78}$/C, and $Pd_{0.38}$/C.

Open Access Article. Published on 08 October 2025. Downloaded on 4/2/2026 11:09:37 PM. This article is licensed under a Creative Commons Attribution-NonCommercial 3.0 Unported Licence.

Table 1 Correlation between the Pd-loading in Pd_x/C and their ORR mass activities determined at 0.85 V *vs.* RHE

Pd loading in Pd_x/C		
Input Pd loading	ICP-OES determined Pd loading	ORR mass activity (A g_{Pd}^{-1}, at 0.85 V *vs.* RHE)
$x = 0.05$	—	—
$x = 0.50$	$x = 0.13$	113
$x = 1.00$	$x = 0.38$	117
$x = 1.96$	$x = 0.78$	110
$x = 3.85$	$x = 1.84$	199

H_2O_2 selectivity of $Pd_{0.027}$–CeO_2/C before and after this ADT. As shown in Fig. S9a, the $E_{1/2}$ exhibits only a minor shift of 40 mV, indicating relatively stable ORR activity. However, a substantial decrease in the ring current was observed (Fig. S9b), suggesting a notable change in the reaction pathway. This is evidenced by the significant increase in n from nearly 2 (ideal for selective H_2O_2 production) to ~3.5 after the ADT (Fig. S9c). Consequently, both the selectivity and *FE* for H_2O_2 production decrease significantly – from initial values of 97.0% and 94.2% to 25.8% and 14.8%, respectively, at 0.7 V *vs.* RHE (see Table S5 for full details). This substantial shift in n suggests a change in the dominant reaction pathways, which is unfavorable for H_2O_2 production and may be attributed to an increase in Pd ensemble sites after cycling. The estimated molar H_2O_2 production rate after ADT at 0.7 V *vs.* RHE is 39.5 mol g_{Pd}^{-1} h^{-1}, which corresponds to ~20% of its initial value and ~47% of the initial rate achieved by the Pd_{10}/C commercial catalyst (Table S2). Further optimization of Pd anchoring in the low-loading regime could not only prevent degradation in H_2O_2 selectivity but also enhance the production rate over prolonged catalytic operation.

Validation of metal–support interaction

The observed H_2O_2 production performance may theoretically arise from any of the following MSIs: Pd(PdO)/CeO_2, CeO_2/C, or Pd(PdO)/C. To investigate the individual contributions, we further conducted a series of control experiments. To rule out the potential contribution of Pd-carbon MSI to the overall catalytic performance, we explored an alternative synthesis strategy, referred to as the "pre-loading" method. In this approach, Pd^{2+} was first reduced on CeO_2 NCs to form Pd-based clusters on CeO_2 nano-substrate, which were then loaded onto activated carbon. The resulting catalysts, with similar overall composition, were designated as "$Pd_x^{'} - CeO_2/C$". This strategy was intended to maximize Pd-loading on the CeO_2 substrate and prevent direct deposition of Pd onto the carbon support. However, experimental results revealed that the ORR performance of $Pd_x^{'} - CeO_2/C$ was inferior to that of Pd_x–CeO_2/C synthesized *via* the established method described earlier, despite identical Pd loadings. For example, Fig. S10 compares the ORR polarization curves of $Pd_{0.76}^{'} - CeO_2/C$ and $Pd_{0.76}$–CeO_2/C, showing mass activities of 1.52 A g_{Pd}^{-1} and 624 A g_{Pd}^{-1} at 0.85 V *vs.* RHE, respectively. This clearly demonstrates that the "pre-loading" method results in significantly lower catalytic performance. We also evaluated CeO_2/C as a baseline catalyst to assess its intrinsic performance, although previous studies have shown that the H_2O_2 selectivity (83%) and production rate (4.6 mol g^{-1} h^{-1}) of pristine CeO_2 NCs are significantly lower than those of $Pd_{0.027}$–CeO_2/C.[26] As shown in Fig. S4c, CeO_2/C exhibits negligible ORR activity, with an estimated mass activity of ~0.2 A g^{-1} at 0.85 V only, which is insignificant compared to the Pd-containing samples.

In a separate effort to isolate the influence of Pd–carbon MSI, we prepared a control set of samples by directly depositing Pd clusters onto carbon black, followed by annealing at 300 °C for 30 minutes. These samples were labeled as Pd_x/C, with Pd loadings of $x = 0.05$, 0.13, 0.38, 0.78, and 1.84 wt%. However, XRD analysis revealed that this process led to the formation of Pd NPs rather than clusters in most cases. Specifically, Fig. 5 shows the appearance of distinct metallic Pd peaks at $2\theta = 40.119°$ and 46.659° when the Pd loading reached 0.13 wt% or higher. As expected from the XRD results, the ORR performance of these carbon-supported Pd samples was generally inferior to that of the Pd_x–CeO_2/C catalysts. For instance, Fig. S4a compares the CV profiles of $Pd_{1.84}$/C and $Pd_{1.53}$–CeO_2/C after ~50 potential cycles. A prominent reduction peak at 0.675 V *vs.* RHE is observed in $Pd_{1.84}$/C during the negative sweep (from 1.2 V to 0.1 V), which is absent in $Pd_{1.53}$–CeO_2/C. This suggests that the catalytic activity observed at that potential in $Pd_{1.84}$/C may be associated with Pd NCs on the carbon substrate. Furthermore, as shown in Fig. S4c, the ORR polarization curves of pristine CeO_2/C and the Pd_x/C series were compared with those of Pd_x–CeO_2/C and the benchmark Pd_{10}/C. The Pd_x/C samples exhibited lower $\Delta E_{1/2}$ values and, therefore, poorer H_2O_2 production activity, highlighting their less favorable catalytic behavior. The ORR experiments conducted in O_2-saturated 1 M KOH confirmed these trends, and the corresponding mass activities at 0.85 V are summarized in Table 1. Collectively, these results confirm that the Pd_x–CeO_2/C catalysts, which leverage the synergistic MSI between both Pd–CeO_2 and Pd–C interfaces, represent an optimized design. This dual-interface configuration results in superior H_2O_2 production performance compared to any single-component Pd-based system, including Pd_x/C or $Pd_{0.76}^{'} - CeO_2/C$.

Conclusions

This study presents a straightforward and effective strategy for synthesizing PdO clusters that exist in their oxidized state and serve as active electrocatalysts for H_2O_2 production. By carefully

 This journal is © The Royal Society of Chemistry 2025

Open Access Article. Published on 08 October 2025. Downloaded on 4/2/2026 11:09:37 PM. This article is licensed under a Creative Commons Attribution-NonCommercial 3.0 Unported Licence.

optimizing the synthesis and loading procedures, PdO clusters were successfully anchored on carbon-supported CeO_2 nanosubstrates, yielding catalytically active hybrid materials. Among the various formulations, Pd_x–CeO_2/C catalysts with Pd loadings up to 0.35 wt% exhibited significantly enhanced mass activity in alkaline media compared to both high-loading Pd_x–CeO_2/C variants and the benchmark Pd (10 wt%)/C catalyst, while also maintaining comparable electrochemical stability under potential cycling conditions. Notably, the low-Pd-loading sample $Pd_{0.027}$–CeO_2/C exhibited outstanding performance, achieving 97.0% H_2O_2 selectivity and 94.2% faradaic efficiency at 0.7 V *vs.* RHE, along with a peak H_2O_2 molar production rate of 195.8 mol g_{Pd}^{-1} h^{-1}. These outstanding performances are attributed to synergistic interactions among the high density of isolated Pd clusters, CeO_2 NCs, and the carbon support, which collectively enhance catalytic efficiency through oxygen bonding along the 2e-ORR pathway. We also identified that the potential cycling process (*i.e.*, ADT) not only enhances the tendency for cluster/NC agglomeration but may also cause mass transfer from small NCs or clusters to larger agglomerated groups, resembling a coarsening process. This work highlights the potential of PdO–CeO_2–carbon MSI composite catalysts for scalable H_2O_2 electrosynthesis, while also revealing that improving their stability remains a key challenge. It provides a strong foundation for the rational design of next-generation integrated catalytic systems that combine metal clusters, oxides, and carbon supports.

Author contributions

P. B.: conceptualization, investigation, methodology, formal analysis, data curation, writing – original draft. C. L.: conceptualization, methodology, formal analysis, data curation, validation, writing – review & edition. B. Z.: investigation. A. D.: investigation. L. Z.: methodology, investigation, data curation. J. F.: conceptualization, funding acquisition, project administration, supervision, manuscript revision & edition. All authors discussed the results and reviewed the manuscript.

Conflicts of interest

There are no conflicts to declare.

Data availability

The data supporting this article have been included as part of the supplementary information (SI). Supplementary information: includes supplementary figures (electron microscopic images of the $Pd_{1.53}$–CeO_2/C sample, TEM images of individual CeO_2 substrates without Pd element and carbon, XRD patterns of Pd_x–CeO_2/C composites, electrochemical characterizations of Pd_x–CeO_2/C, ORR polarization disc and ring currents of Pd_x–CeO_2/C and Pd_{10}/C determined in 1 M KOH, HAADF-STEM images and EDX elemental maps of $Pd_{0.76}$–CeO_2/C and $Pd_{1.53}$–CeO_2/C catalysts after 5000-cycle ADT, HRTEM images and corresponding data analysis of $Pd_{1.53}$-CeO_2/C before and after ADT, HRTEM images of $Pd_{1.53}$–CeO_2/C after 5000-cycle ADT, RRDE measurements of $Pd_{0.027}$–CeO_2/C before and after 5000-cycle ADT in 1 M KOH, and comparison of ORR polarization curves of sample $Pd_{0.76}$–CeO_2/C and $Pd'_{0.76}$–CeO_2/C generated *via* the "pre-loading" method), supplementary tables (Pd loadings of the input set and actual loadings determined by ICP-OES analysis, H_2O_2 production yield and molar rate estimated from the ring current, comparison of H_2O_2 production performance across various metal-based electrocatalysts, mass activity loss of Pd_x–CeO_2/C and Pd_{10}/C after 5000 potential cycles, and comparison of H_2O_2 yield on $Pd_{0.027}$–CeO_2/C before and after 5000-cycle ADT conducted in 1 M KOH), and related references. See DOI: **https://doi.org/10.1039/d5ta05763a**.

Acknowledgements

P. B. gratefully acknowledges partial support from the National Science Foundation (NSF) under Grant No. DMR-2347030. L. Z. acknowledges use of the Thermo Fisher Talos 200X at the Center for Functional Nanomaterials, which is a U.S. Department of Energy (DOE) Office of Science User Facility, at Brookhaven National Laboratory under Contract No. DE-SC0012704. We thank Dr In-Tae Bae, Dr Stephen Cain, and Dr Anju Sharma for their training and assistance with TEM and XPS analysis in the Analytical and Diagnostics Lab (ADL). We also acknowledge Dr Clament Sagaya Selvam for valuable discussion, and Dr Jinfong Pan, Konakanchi Gayatri Ramesh, and Brendan Groth for their contributions to the experimental work. Support for TEM imaging was provided at S3IP/ADL at the State University of New York at Binghamton and the College of Arts & Sciences Microscopy at Texas Tech University.

References

1 R. Ciriminna, L. Albanese, F. Meneguzzo and M. Pagliaro, *ChemSusChem*, 2016, **9**, 3374–3381.
2 H. Pouri, R. Panta, P. Bharathan, J. Fang and J. Zhang, *Micro*, 2025, **5**, 15.
3 K. P. Bryliakov, *Chem. Rev.*, 2017, **117**, 11406–11459.
4 J. M. Campos-Martin, G. Blanco-Brieva and J. L. G. Fierro, *Angew. Chem., Int. Ed.*, 2006, **45**, 6962–6984.
5 J. K. Edwards, S. J. Freakley, R. J. Lewis, J. C. Pritchard and G. J. Hutchings, *Catal. Today*, 2015, **248**, 3–9.
6 C. Xia, Y. Xia, P. Zhu, L. Fan and H. Wang, *Science*, 2019, **366**, 226–231.
7 Q. Chang, P. Zhang, A. H. B. Mostaghimi, X. Zhao, S. R. Denny, J. H. Lee, H. Gao, Y. Zhang, H. L. Xin, S. Siahrostami, J. G. Chen and Z. Chen, *Nat. Commun.*, 2020, **11**, 2178.
8 Z. Lu, G. Chen, S. Siahrostami, Z. Chen, K. Liu, J. Xie, L. Liao, T. Wu, D. Lin, Y. Liu, T. F. Jaramillo, J. K. Nørskov and Y. Cui, *Nat. Catal.*, 2018, **1**, 156–162.
9 M. Dan, R. Zhong, S. Hu, H. Wu, Y. Zhou and Z.-Q. Liu, *Chem Catal.*, 2022, **2**, 1919–1960.
10 J. S. Jirkovský, I. Panas, E. Ahlberg, M. Halasa, S. Romani and D. J. Schiffrin, *J. Am. Chem. Soc.*, 2011, **133**, 19432–19441.

Open Access Article. Published on 08 October 2025. Downloaded on 4/2/2026 11:09:37 PM. This article is licensed under a Creative Commons Attribution-NonCommercial 3.0 Unported Licence.

11 E. Pizzutilo, O. Kasian, C. H. Choi, S. Cherevko, G. J. Hutchings, K. J. J. Mayrhofer and S. J. Freakley, *Chem. Phys. Lett.*, 2017, **683**, 436–442.
12 A. Verdaguer-Casadevall, D. Deiana, M. Karamad, S. Siahrostami, P. Malacrida, T. W. Hansen, J. Rossmeisl, I. Chorkendorff and I. E. L. Stephens, *Nano Lett.*, 2014, **14**, 1603–1608.
13 J. Kim, H.-E. Kim and H. Lee, *ChemSusChem*, 2018, **11**, 104–113.
14 B. Qiao, A. Wang, X. Yang, L. F. Allard, Z. Jiang, Y. Cui, J. Liu, J. Li and T. Zhang, *Nat. Chem.*, 2011, **3**, 634–641.
15 H.-E. Kim, I. H. Lee, J. Cho, S. Shin, H. C. Ham, J. Y. Kim and H. Lee, *ChemElectroChem*, 2019, **6**, 4757–4764.
16 K. Rigby, D. Huang, D. Leshchev, H. J. Lim, H. Choi, A. F. Meese, S. Weon, E. Stavitski and J.-H. Kim, *Environ. Sci. Technol.*, 2023, **57**, 13681–13690.
17 J. Li, Q. Hou, X. Pei, L. Wang, F. Liu, M. Ran and T. Dai, *J. Mol. Struct.*, 2024, **1316**, 139081.
18 S. Yu, X. Cheng, Y. Wang, B. Xiao, Y. Xing, J. Ren, Y. Lu, H. Li, C. Zhuang and G. Chen, *Nat. Commun.*, 2022, **13**, 4737.
19 Z. Wei, B. Deng, P. Chen, T. Zhao and S. Zhao, *Chem. Eng. J.*, 2022, **428**, 131112.
20 J. S. Choi, S. Yoo, E. S. Koh, R. Aymerich-Armengol, C. Scheu, G. V. Fortunato, M. R. V. Lanza, Y. J. Hwang and M. Ledendecker, *Adv. Mater. Interfaces*, 2023, **10**, 2300647.
21 K. Qi, M. Chhowalla and D. Voiry, *Mater. Today*, 2020, **40**, 173–192.
22 T. W. van Deelen, C. Hernández Mejía and K. P. de Jong, *Nat. Catal.*, 2019, **2**, 955–970.
23 G. N. Vayssilov, Y. Lykhach, A. Migani, T. Staudt, G. P. Petrova, N. Tsud, T. Skála, A. Bruix, F. Illas, K. C. Prince, V. Matolin, K. M. Neyman and J. Libuda, *Nat. Mater.*, 2011, **10**, 310–315.
24 X. Li, X. I. Pereira-Hernández, Y. Chen, J. Xu, J. Zhao, C.-W. Pao, C.-Y. Fang, J. Zeng, Y. Wang, B. C. Gates and J. Liu, *Nature*, 2022, **611**, 284–288.
25 C. Wang, X.-K. Gu, H. Yan, Y. Lin, J. Li, D. Liu, W.-X. Li and J. Lu, *ACS Catal.*, 2017, **7**, 887–891.
26 M. Cheng, Z. Li, T. Xu, Y. Mao, Y. Zhang, G. Zhang and Z. Yan, *Electrochim. Acta*, 2022, **430**, 141091.
27 C. Li, Y. Luan, B. Zhao, A. Kumbhar, F. Zhang and J. Fang, *MRS Adv.*, 2020, **5**, 523–529.
28 S. Yang and L. Gao, *J. Am. Chem. Soc.*, 2006, **128**, 9330–9331.
29 C. Li, S. Kwon, X. Chen, L. Zhang, A. Sharma, S. Jiang, H. Zhang, M. Zhou, J. Pan, G. Zhou, W. A. Goddard III and J. Fang, *Nano Lett.*, 2023, **23**, 3476–3483.
30 Y. Wu, S. Geng, J. Liu, Y. Liu, K. Wang, Y. Wang and S. Song, *Angew. Chem., Int. Ed.*, 2025, **64**, e202505699.
31 Y. Yang, Y. Xiong, M. E. Holtz, X. Feng, R. Zeng, G. Chen, F. J. DiSalvo, D. A. Muller and H. D. Abruña, *Proc. Natl. Acad. Sci. U. S. A.*, 2019, **116**, 24425–24432.
32 B. N. Ruggiero, X. K. Lu, B. Lu, A. E. Deberghes, D. Nordlund, J. M. Notestein and L. C. Seitz, *J. Mater. Chem. A*, 2024, **12**, 27311–27326.
33 F. Jiang, S. Wang, B. Liu, J. Liu, L. Wang, Y. Xiao, Y. Xu and X. Liu, *ACS Catal.*, 2020, **10**, 11493–11509.
34 P. Th, R. Zimmermann, P. Steiner and S. Hüfner, *J. Phys.: Condens. Matter*, 1997, **9**, 3987.
35 X. Mao, M. Ou, W. Zhao, M. Shi and L. Zheng, *Nanotechnology*, 2024, **35**, 475701.
36 N. M. Wilson and D. W. Flaherty, *J. Am. Chem. Soc.*, 2016, **138**, 574–586.
37 R. Liu, C. Wang, Y. Yan, R. Wang and G. Chen, *ACS Catal.*, 2024, **14**, 3955–3965.
38 M. Chai, R.-J. Xing, J. Chen, Z.-X. Su, H. Wei, H.-W. Zhu and X.-Q. Gong, *ACS Sustainable Chem. Eng.*, 2025, **13**, 1391–1400.
39 X. Wang, H. Xu, Y. Luo and D. Cheng, *ChemCatChem*, 2022, **14**, e202200853.
40 K. Jiang, S. Back, A. J. Akey, C. Xia, Y. Hu, W. Liang, D. Schaak, E. Stavitski, J. K. Nørskov, S. Siahrostami and H. Wang, *Nat. Commun.*, 2019, **10**, 3997.
41 B.-W. Zhang, T. Zheng, Y.-X. Wang, Y. Du, S.-Q. Chu, Z. Xia, R. Amal, S.-X. Dou and L. Dai, *Commun. Chem.*, 2022, **5**, 43.
42 J. Du, S. Jiang, R. Zhang, P. Wang, C. Ma, R. Zhao, C. Cui, Y. Zhang and Y. Kang, *ACS Catal.*, 2023, **13**, 6887–6892.
43 E. Jung, H. Shin, B.-H. Lee, V. Efremov, S. Lee, H. S. Lee, J. Kim, W. Hooch Antink, S. Park, K.-S. Lee, S.-P. Cho, J. S. Yoo, Y.-E. Sung and T. Hyeon, *Nat. Mater.*, 2020, **19**, 436–442.
44 B.-Q. Li, C.-X. Zhao, J.-N. Liu and Q. Zhang, *Adv. Mater.*, 2019, **31**, 1808173.
45 T. W. Hansen, A. T. DeLaRiva, S. R. Challa and A. K. Datye, *Acc. Chem. Res.*, 2013, **46**, 1720–1730.

 This journal is © The Royal Society of Chemistry 2025